Electronic Supplementary Material (ESI) for RSC Advances.
This journal is © The Royal Society of Chemistry 2020

Electronic Supplementary Information

Amino-1H-Tetrazole-Regulated High-Density Nitrogen-Doped Hollow Carbon Nanospheres for Long-Life Zn-Air Batteries

Shizhu Song [a, 1], Tao Yang [a, 1], Rongwei Shi [b], and Qi Li [a,c] *

[a] School of Chemistry and Chemical Engineering, Nantong University, Nantong, 226019, Jiangsu, P. R. China

[b] School of Material and Chemical Engineering, Tongren University, Tongren, 554300, Guizhou, P. R. China

[c] Nantong Key Lab of Intelligent and New Energy Materials, Nantong University, Nantong, 226019, Jiangsu, P. R. China

[1]These authors contributed equally to this work.

Corresponding author: Dr. Qi Li, E-mail: zhuiqiuzhizhuo@163.com

*Corresponding authors: Qi Li, zhuiqiuzhizhuo@163.com

Experimental Section

Chemicals and Regents

Pyrrole (C_4H_5N, CP), styrene (C_8H_8, >99.5%), amino-1H-tetrazole (CH_3N_5, >99.0%), sodium dodecyl sulfate (SDS, >99.0%), were purchased from Aladdin chemistry Co., Ltd.. Pyrrole and styrene monomer were distilled under reduced pressure before use. Pt/C (40%, JM) powders (HiSPEC 3000) were obtained from Alfa Aesar. Thiourea (CH_4N_2S, >99.0%), sodium carbonate (Na_2CO_3, >98.0%), potassium persulfate ($K_2S_2O_8$, >99.0%), sodium persulfate ($(NH_4)_2S_2O_8$, >98.0%), polyvinyl alcohol (PVA) were purchased from Sinopharm Chemicals Co., Ltd.. Potassium hydroxide (KOH, >95.0%), sulfuric acid (H_2SO_4, >98.0%), methanol (CH_3OH, >99.5%), ethanol (C_2H_5OH, >99.0%) were provided by Xilong Chemical Reagent Co., Ltd.. Distilled deionized water (>18.2 MΩ) was produced by reverse osmosis followed by ion-exchange and filtration (HBI, Shenzhen Honbo Water Treatment Equipment Co., Ltd., China). All chemicals and regents were used without further purification apart from pyrrole and styrene.

Synthesis of negatively charged polystyrene (PS) nanospheres

PS dispersion was synthesized via a modified emulsion polymerization method according to our previous work. In brief, anhydrous Na_2CO_3 (0.1 g, 0.94 mmol) and SDS (0.2 g, 0.69 mmol) were dissolved into 300 mL distilled water, then transferred them into a round-bottom flask and purging with N_2 for 30 min. Subsequently, styrene (30 mL) was added rapidly, keeping intense agitation for 30 min at 60 ℃. Finally, pouring the $K_2S_2O_8$ aqueous solution (10 mL, 1 mmol) into the above reaction system, heated to 75 ℃, and keeping for 20 h. After cooling down to room temperature, the products were centrifuged at 15000 rpm for 30 min for several times with distilled water. The

as-obtained PS nanospheres were re-dispersed in 90 mL distilled water, and was denoted PS mother solution.

Synthesis of protonated graphitic carbon nitride (P-g-C_3N_4) nanosheets

Bulk g-C_3N_4 powder was used to synthesize the P-g-C_3N_4 nanosheets. In brief, thiourea (5.0 g) was encapsulated into the corundum crucible with a lid, then the crucible was placed in tubular furnace, followed by a heat treatment from room temperature to 550 ℃ (keeping for 2 h) with a heating rate of 2.3 ℃ min^{-1} in N_2 flow. After cooling down to room temperature, the products were grinded thoroughly with an agate mortar, and was denoted as bulk g-C_3N_4. For the synthesis of P-g-C_3N_4, bulk g-C_3N_4 (200 mg) powder was added into a 500 mL round flask containing the mixed concentrated sulfuric acid and nitric acid (40 mL) with a volume ratio of 1:3. Afterwards, the round flask was sonicated severely until the solution is clear. Pouring deionized water (400 mL) into the clear solution to form a dispersion of P-g-C_3N_4 nanosheets. After the centrifugation by using deionized water at 10000 rpm for several times, the as-obtained product was collected, and was denoted P-g-C_3N_4.

Synthesis of PS@P-g-C_3N_4-ATTZ@PPy precursor

Briefly, PS mother solution (2 mL) was dispersed into a beaker containing 100 mL deionized water, then P-g-C_3N_4 (100 mg) and ATTZ (50 mg) were added to generate homogeneous dispersion. Subsequently, 0.1 mL pyrrole monomer was added to the above system under stirring, accompanied by a polymerization process via adding the potassium persulfate solution (20 mmol L^{-1}, 20 mL) drop by drop. After four hours of polymerization, the mixture was filtered and washed with deionized water and ethanol several times. Finally, the product was dried at 60 ℃ vacuum oven over the night,

which denotes as PS@P-g-C_3N_4-ATTZ@PPy. For better understanding the effect of nitrogen content on ORR, a series of PS@P-g-C_3N_4-ATTZ@PPy precursors were prepared in the same way excepting for different amounts of ATTZ (100, 150, 200, 250 mg).

Synthesis of high-density graphitic and pyridinic nitrogen-doped hollow carbon nanospheres (G&P N-HCS)

The as-obtained several precursors was carbonized at 950 ℃ with a heating rate of 5 ℃ min^{-1} for 2 h under N_2 flowing, which denotes as G&P N-HCS. Notably, different amounts of ATTZ derived G&P N-HCS products were denoted G&P N-HCSx (x refer to the weight ratio of P-g-C_3N_4 and ATTZ). For example, as the amount of ATTZ to be 50 mg (ATTZ : P-g-C_3N_4=1:2), the as-prepared product was denoted G&P N-HCS1. Other products were denoted G&P N-HCS2, G&P N-HCS3, G&P N-HCS4, and G&P N-HCS5 successively. In particular, when the ATTZ is absent, the corresponding product was denoted N-HCS. The product derived from PPy denoted as HCS.

Characterization

Field emission scanning electron microscopy (FESEM) images were performed by a Gemini SEM 300. Transmission electron microscopic (TEM) images and energy dispersive spectroscopy (EDS) mappings were analyzed using a Tecnai G2 F20 at 200 kV. Powder X-ray diffraction (XRD) patterns were collected on a Philips X'pert PRO with nickel-fleered Cu K_α radiation. Raman spectra were carried out using a LabRAM HR800 with an excitation wavelength of 532 nm. The chemical composition and environment were conducted on an X-ray photoelectron spectroscopic (XPS, Shimadzu ESCA-3400) using an Mg K_α source. N_2 adsorption/desorption isotherms were recorded on a Micromeritics ASAP 2020 instrument using a Brunauer-Emmett-Teller (BET) method at 77 K.

Pore-size distributions (PSD) were measured by using the non-localized density functional theory (NLDFT) method. Mesopore volumes were calculated by Barrett, Joyner and Halenda (BJH) method. The elemental contents of catalysts were performed by Elemental analyzer (EA).

Electrochemical Measurements

The ORR performances were conducted by using an electrochemical workstation (CHI760E, Shanghai, Chenhua, Co., Ltd.) equipped with a three-electrode system in 0.1 M KOH electrolyte. The ORR activity was measured by using rotation disk electrode (RDE) and rotation ring-disk electrode (RRDE) technologies. The catalysts inks were prepared as follows. The as-prepared catalyst (16 mg) was added to a Schering bottles (20 mL) containing 5 wt.% Nafion solution (160 μL), deionized water (3 mL), and isopropanol (1 mL), then the reactor was sonicated for at least 30 min to form a homogenous ink. The catalyst ink (15 μL) was drop-casted onto a glass carbon electrode (5 mm in diameter) and dried at 30 ℃ for 12 h successively, then denote as working electrode. The loading of catalysts is controlled to be 0.3 mg cm^{-2} for all samples in the same way. For comparison, the JM Pt/C (40 wt.%) benchmark catalyst with the same loading amount was also fabricated. An Pt ring used as the counter electrode and a Ag/AgCl electrode (saturated KCl) acted as the reference electrode. All the potentials were calibrated to the reversible hydrogen electrode (RHE) scale according to $E_{vs\ RHE} = E_{vs\ Ag/AgCl} + 0.0591pH + 0.197$.

The activity of glass carbon electrode was verified by using cyclic voltammetry (CV) test with a scanning rate of 50 mV s^{-1} in the electrolyte containing $K_3[Fe(CN)_6]$ (1 mM) and KNO_3 (0.5 M) until the potential difference between oxidation and reduction peaks of $[Fe(CN)_6]^{3-}/[Fe(CN)_6]^{4-}$ redox couple less than 70 mV. O_2 and/or N_2 was ventilated in 0.1 M KOH and/or 0.5 M H_2SO_4 solution at least 30 min to guarantee the saturation of electrolyte before each test. For ORR, CV

tests were conducted at different scanning rate (10, 20, 50, 100, and 200 mV s^{-1}) over a potential window of 0.1-1.1 V (vs. RHE). The kinetics tests were recorded on a linear sweep voltammetry (LSV) technology with a rotation speed range from 225 to 2025 rpm at a scanning rate of 10 mV s^{-1} over a potential window of 0.1-1.1 V (vs. RHE). Tafel slopes were calculated from the Tafel equation:

$$\eta = a + b \log j \quad (1)$$

where η refers to the overpotential, j represents the measured current density, b is the Tafel slope.

For RDE method, the kinetic-limiting current and electron transfer numbers were calculated according to the Koutecky-Levich equation.

$$1/j = 1/j_K + 1/j_L = 1/j_K + 1/(B\omega^{1/2}) \quad (2)$$

$$B = 0.62nFC_0(D_0)^{2/3}\nu^{-1/6} \quad (3)$$

where j is the measured current density, j_K is the kinetic current density, j_L is the diffusion limited current density, ω is the electrode rotation rate, B refers to the reciprocal of slope of the K-L plots, F is Faraday constant (96485 C mol^{-1}), C_0 is the concentration of O_2 (1.2 x 10^{-6} mol cm^{-3}), D_0 represents the diffusion coefficient of O_2 in the electrolyte (1.9 x 10^{-5} cm^2 s^{-1}), and ν is the kinetic viscosity (0.01 cm^2 s^{-1}).

For RRDE method, the LSV tests were carried out in O_2 and/or N_2-saturated electrolyte at a scanning rate of 10 mV s^{-1} under 1600 rpm. The production of H_2O_2 was detected by using LSV measured at 0.5 V vs. RHE. The yield of H_2O_2 and electron transfer number were calculated by the following equations.

$$\%H_2O_2 = 200\frac{I_R/N}{I_D + (I_R/N)} \quad (4)$$

$$n = \frac{4I_D}{I_D + (I_R/N)} \quad (5)$$

where I_D is the measured current density of disk electrode, I_R is the measured current density of Pt ring electrode, N is the current collection efficiency of Pt ring (0.37).

Aqueous Zn-air battery assembly

The as-prepared catalysts were evaluated by using a home-made Zn-air battery device (OMS-T4, Changsha Spring New Energy Technology Co., Ltd., China). Discharge-charge cycling tests were recorded on a LAND testing system (CT2001A, Wuhan, China) with eight channels. Carbon paper was cut into circular with a diameter of 20 mm to be directly acted as the air cathode. A certain amount of the catalyst ink containing the same amount of ruthenium dioxide was casted on the carbon paper with the mass loading of 1.5 ± 0.1mg cm^{-2}. A polished Zn plate with a diameter of 20 mm was used as anode. The electrolyte was prepared by adding 0.2 M $ZnCl_2$ to 6.0 M KOH solution. The membrane adopted a Whatman glass microfiber filter with a diameter of 25 mm. The assembled battery maintained air contact during testing.

Solid Zn-air battery assembly

All as-prepared catalysts casted on carbon paper directly explored as air cathode and the well-polished Zn plate was used as anode. The solid electrolyte was prepared as follows: PVA (3 g), KOH (3 g), and $Zn(CH_3COO)_2$ were dissolved in 24 mL deionized water, then the mixture heated at 90 ℃ under vigorous stirring until the solution become clear. Glass microfiber membrane was soaked in the as-prepared PVA-Zn-KOH electrolyte to obtain the solid electrolyte. Both carbon paper and polished Zn plate with same size were coated each side of the solid electrolyte membrane to fabricate the solid Zn-air battery.

DFT calculations

Structural stability of graphitic N and pyridinic N

Structural models of N species including graphene (G) and N-doped graphene with different ratios of pyridinic and graphitic N (Pr N : Gr N) were constructed to investigate the structure stability. For the seven Gr_N models (denoted as G_0PrN_6GrN, G_1PrN_5GrN, G_2PrN_4GrN, G_3PrN_3CN, G_4PrN_2GrN, G_5PrN_1GrN and G_0PrN_6GrN), the number of pyridinic atoms was set to increase from 0 to 6, meanwhile, the number of graphitic nitrogen atoms changed from 6 to 0. All the geometries were optimized by the B3LYP density functional with the 6-311+g(d) basis set using Gaussian 09 program. Different spin states were also considered to determine the most stable states which were chosen for the calculations of reaction pathways and diagrams analysis of free energy. Moreover, frequency calculations were performed for all the optimized modes to verify the stable structures and to obtain free energies. Zero-point energy and thermal corrections to the total energy were computed within the harmonic approximation using standard expressions of statistical mechanics at 298.15 K. The free energy diagram for the ORR pathway of each stable electrocatalyst model was performed according to the methods mentioned in our previous study.

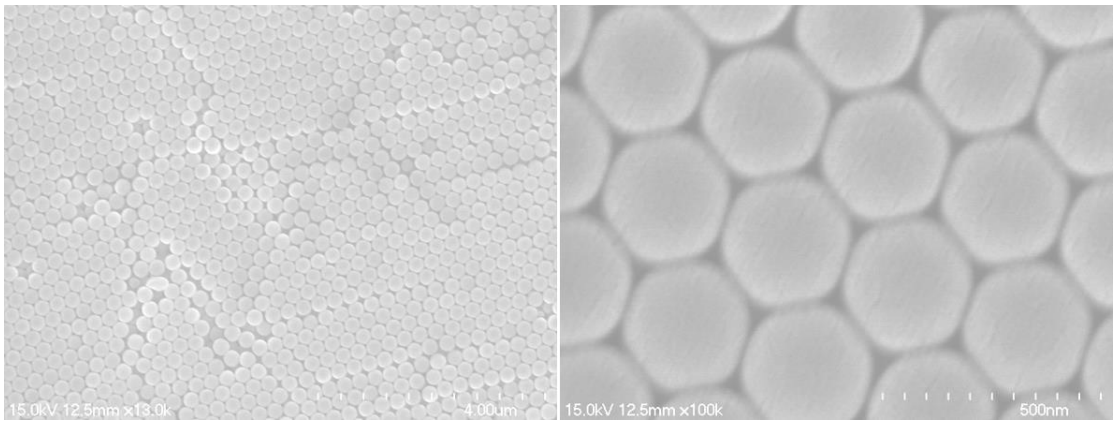

Figure S1. SEM images of PS nanospheres.

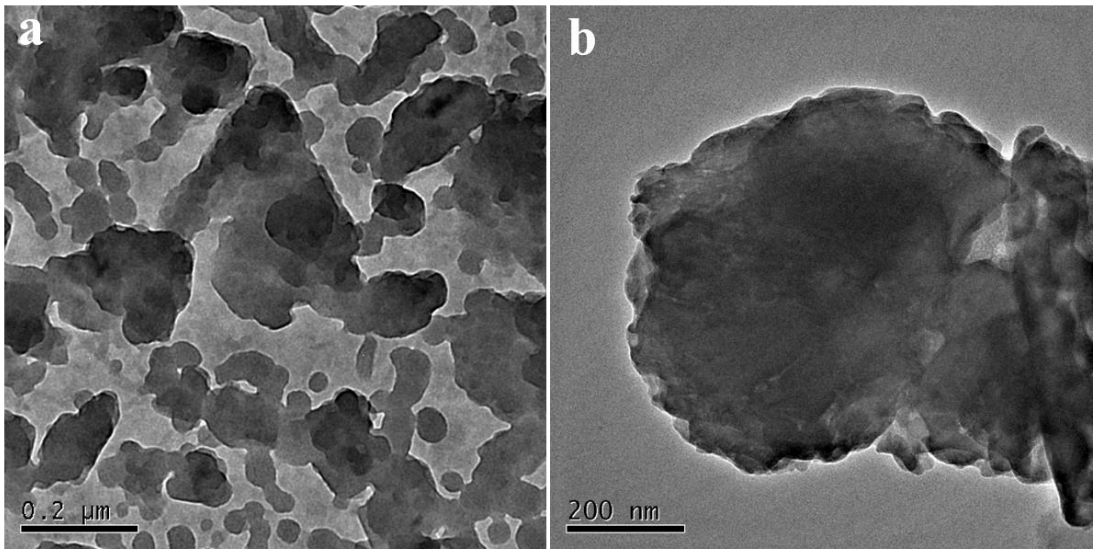

Figure S2. TEM images of P-g-C_3N_4 (a) and bulk g-C_3N_4 (b).

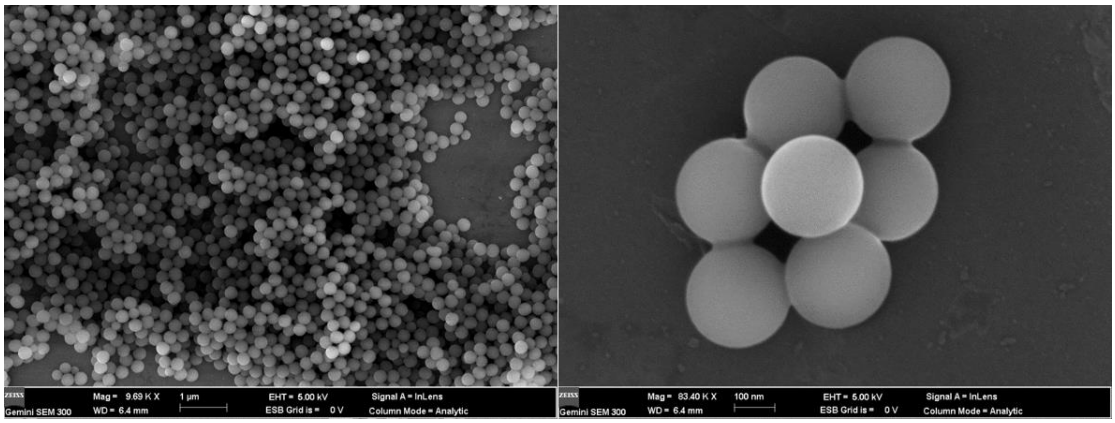

Figure S3. SEM images of PS@P-g-C_3N_4-ATTZ@PPy.

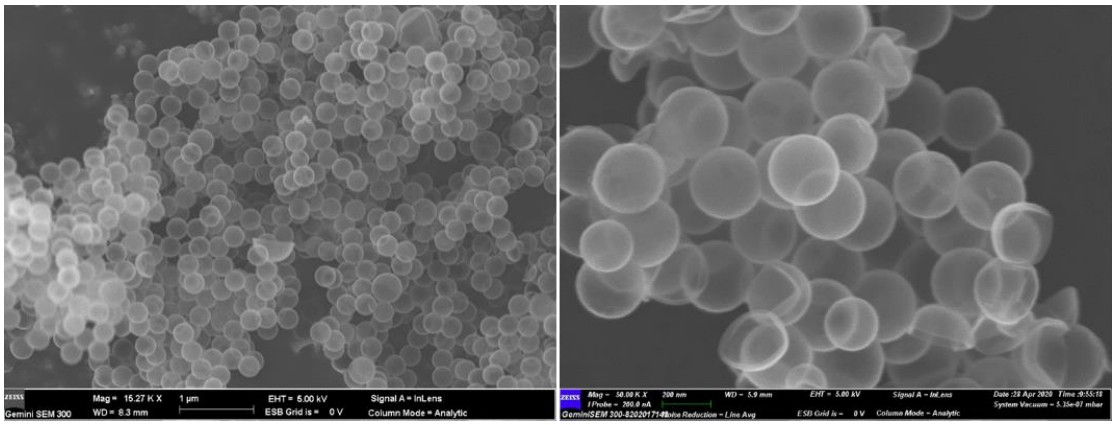

Figure S4. SEM images of G&P N-HCS4.

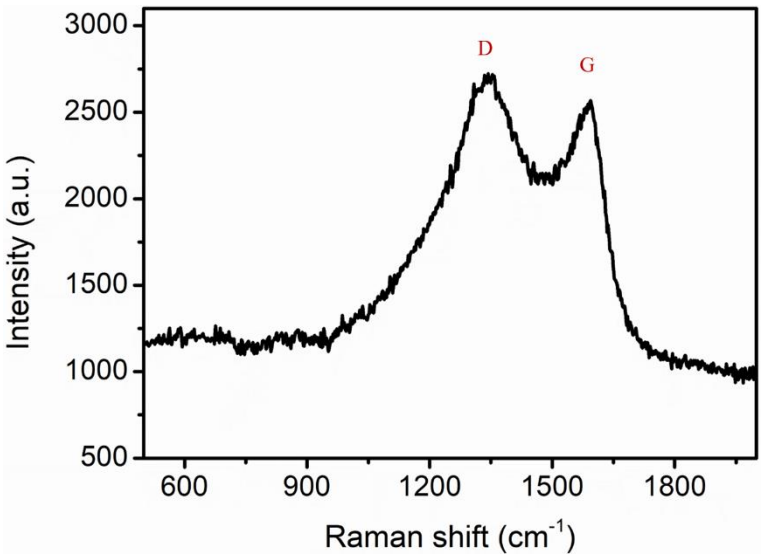

Figure S5. Raman spectrum of G&P N-HCS4.

A higher intensity ratio of G band and D band was observed, suggesting the crystallinity of G&P N-HCS4.

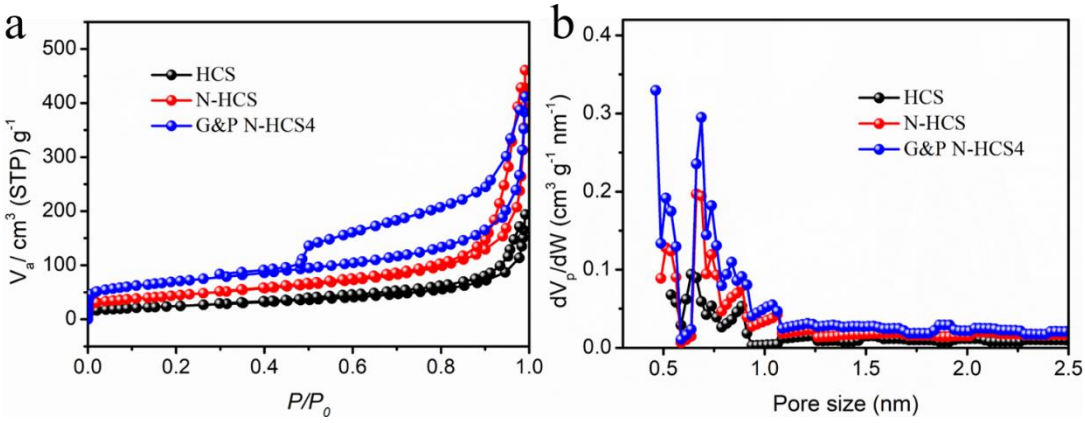

Figure S6. (a) N_2 adsorption/desorption isotherms at 77 K and (b) pore size distribution of HCS, N-HCS, and G&P N-HCS4, respectively.

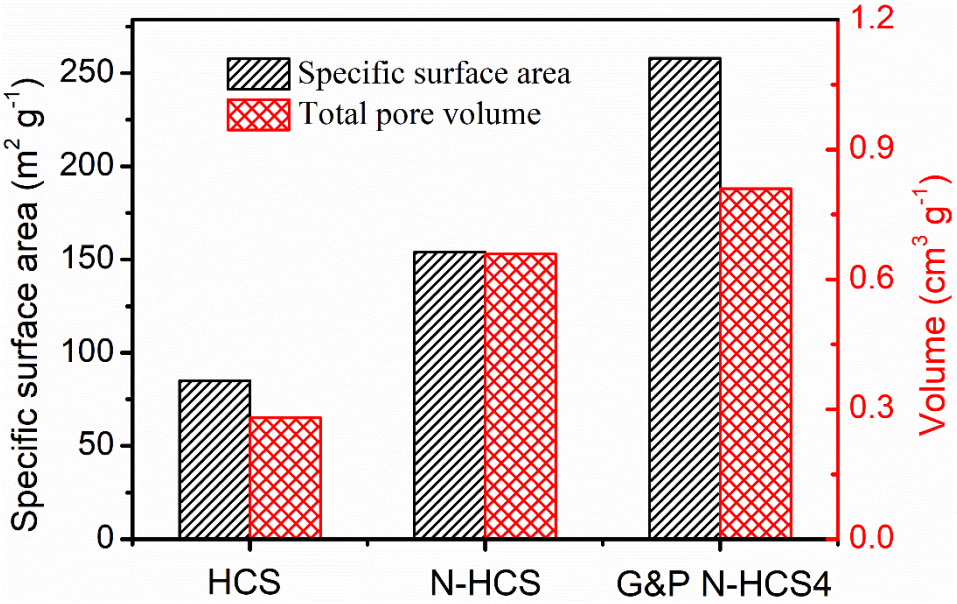

Figure S7. The specific surface area and total pore volume of HCS, N-HCS, and G&P N-HCS4, respectively.

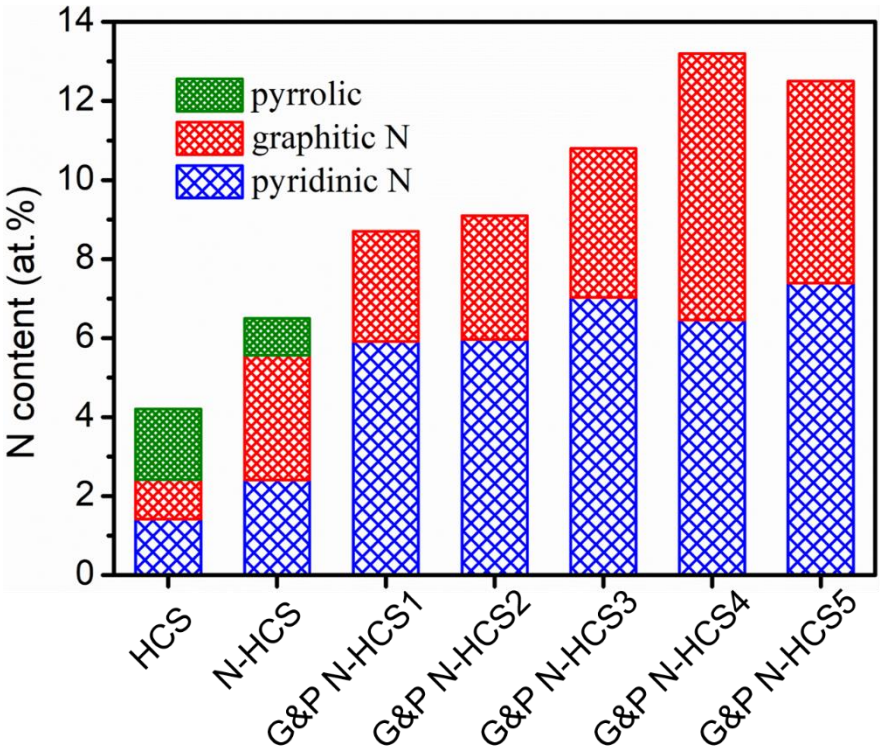

Figure S8. The content of various N types in all samples.

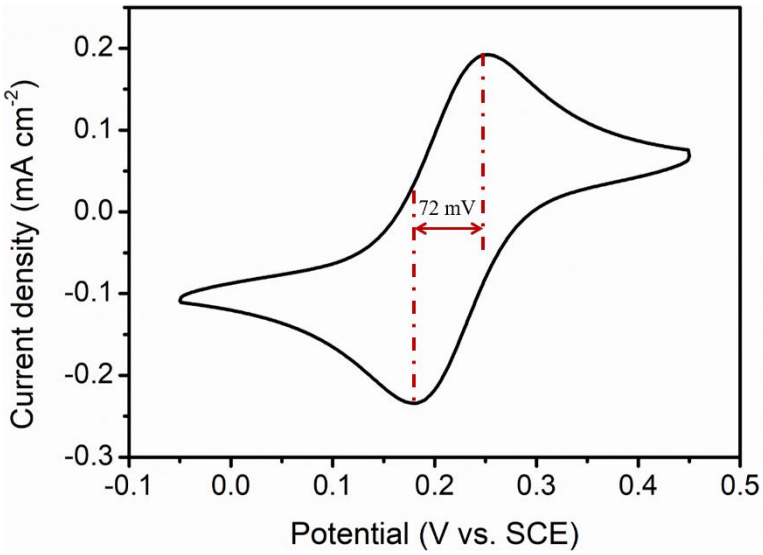

Figure S9. CV curve of the glass carbon electrode tested as $K_3[Fe(CN)_6]/KNO_3$ solution with a reference electrode of Hg/Hg_2Cl_2 and counter electrode of Pt ring.

The potential difference between oxidation peak and cathodic peak, corresponding to $[Fe(CN)_6]^{3-}/[Fe(CN)_6]^{4-}$ redox couple, is close to 70 mV, indicating that the glass carbon electrode is highly reversible.

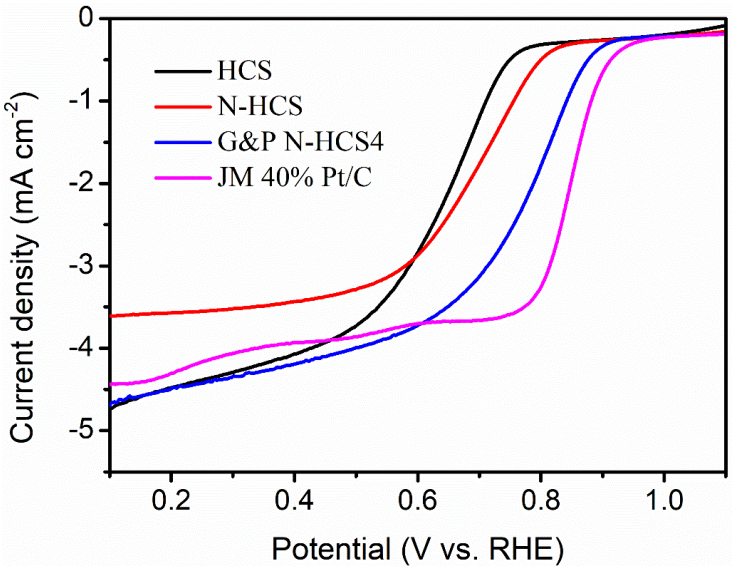

Figure S10. Linear sweep voltammetry (LSV) curves of HCS, N-HCS, G&P N-HCS4, and commercial JM 40% Pt/C under 1600 rpm with a scanning rate of 10 mV s^{-1}.

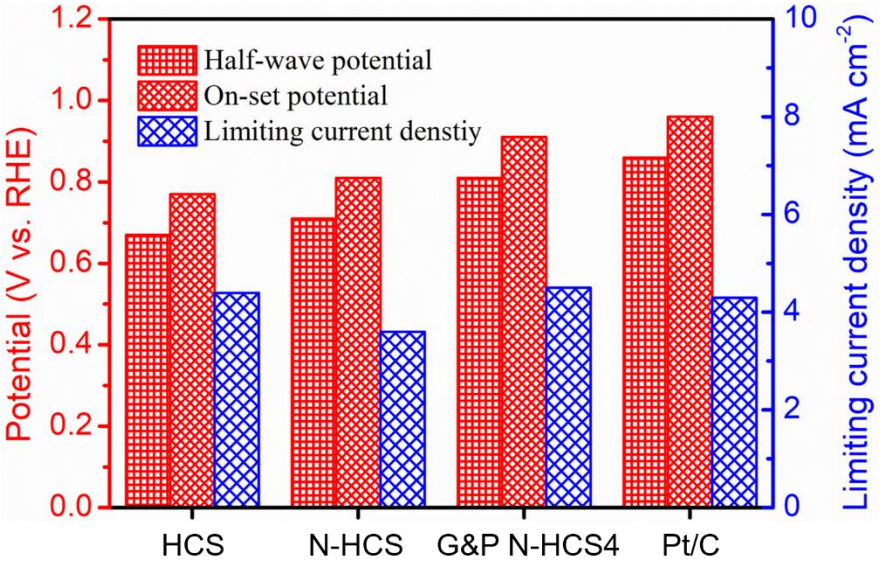

Figure S11. Electrochemical parameters including half-wave potential, on-set potential, and limiting current density of HCS, N-HCS, G&P N-HCS4, and commercial JM 40% Pt/C obtained from the LSV curves.

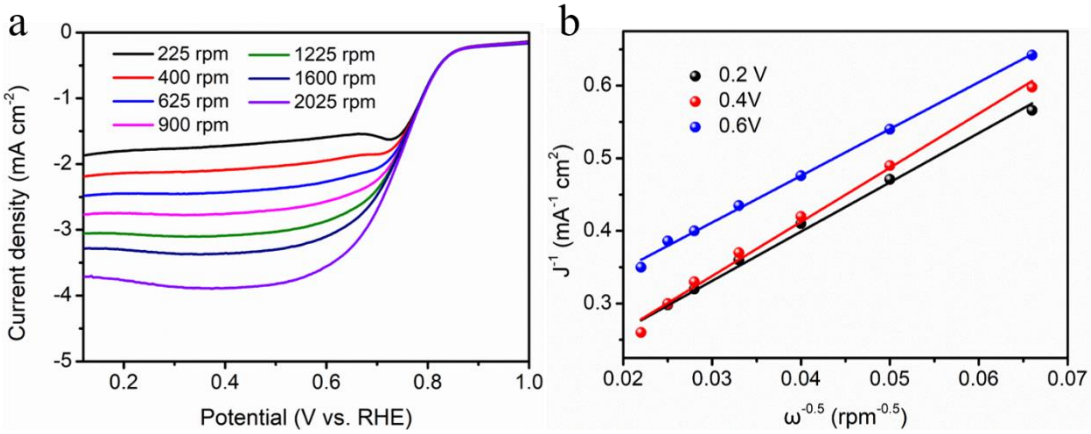

Figure S12. (a) LSV curves at different rotation speeds with a scanning rate of 10 mV s-1 and (b) the corresponding Koutecky-Levich plots at different electrode potential of G&P N-HCS1.

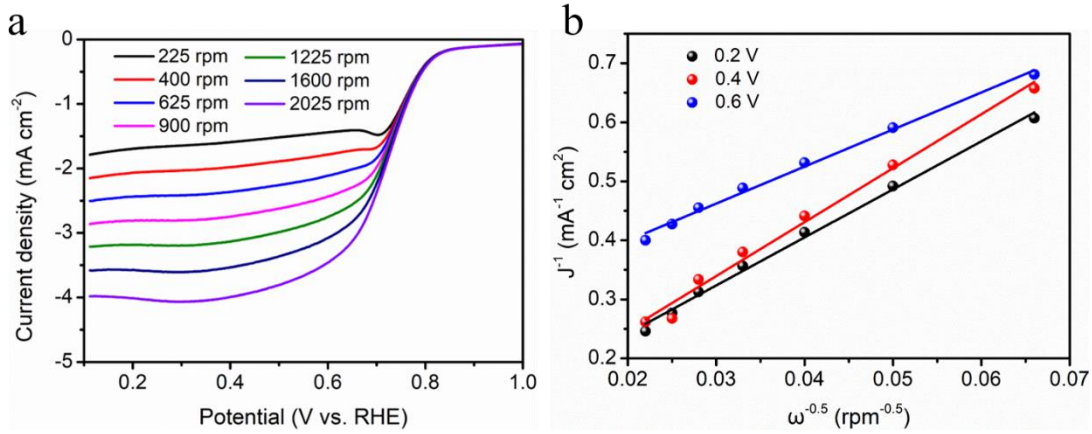

Figure S13. (a) LSV curves at different rotation speeds with a scanning rate of 10 mV s-1 and (b) the corresponding Koutecky-Levich plots at different electrode potential of G&P N-HCS2.

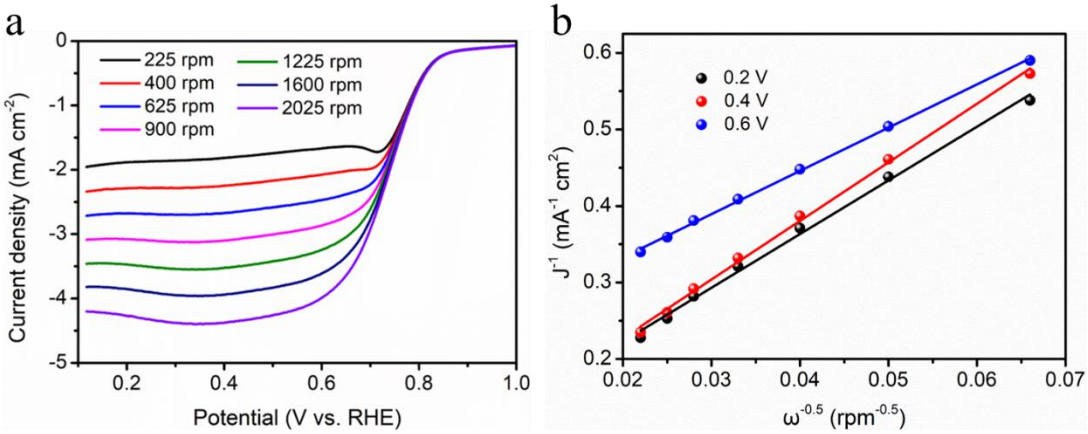

Figure S14. (a) LSV curves at different rotation speeds with a scanning rate of 10 mV s-1 and (b) the corresponding Koutecky-Levich plots at different electrode potential of G&P N-HCS3.

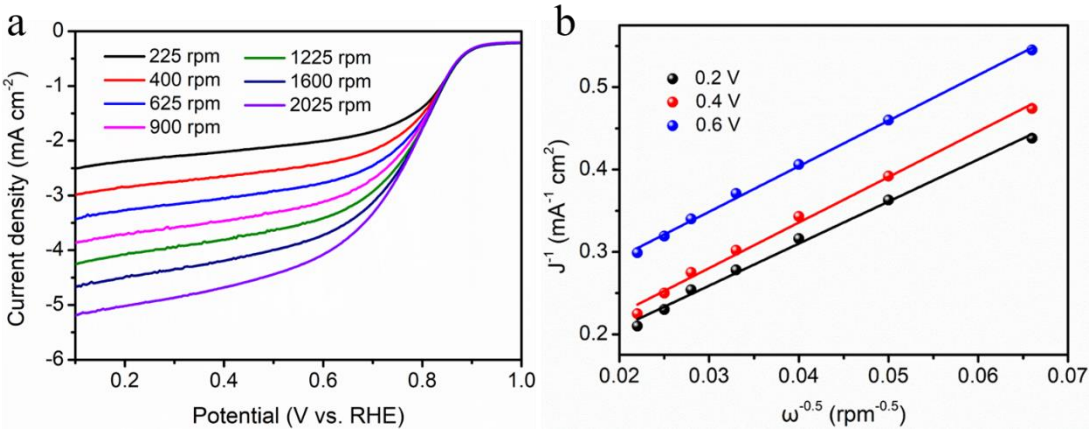

Figure S15. (a) LSV curves at different rotation speeds with a scanning rate of 10 mV s-1 and (b) the corresponding Koutecky-Levich plots at different electrode potential of G&P N-HCS4.

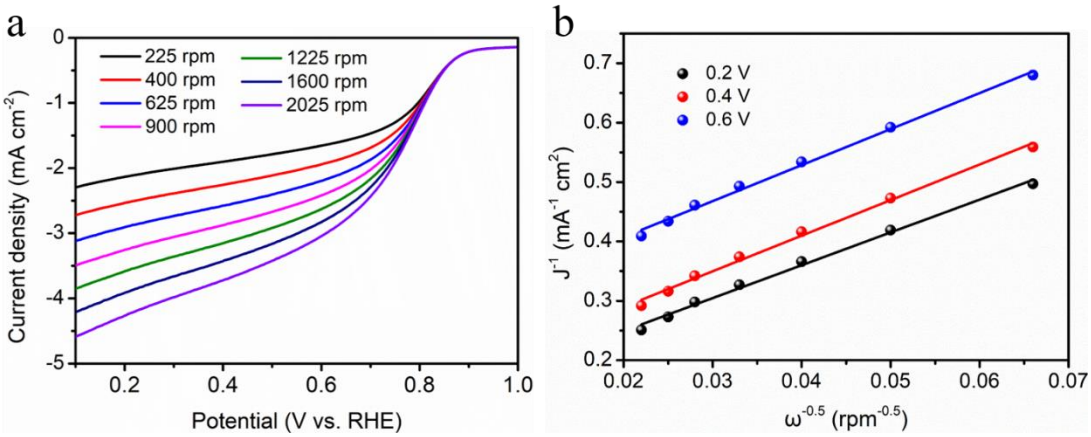

Figure S16. (a) LSV curves at different rotation speeds with a scanning rate of 10 mV s-1 and (b) the corresponding Koutecky-Levich plots at different electrode potential of G&P N-HCS5.

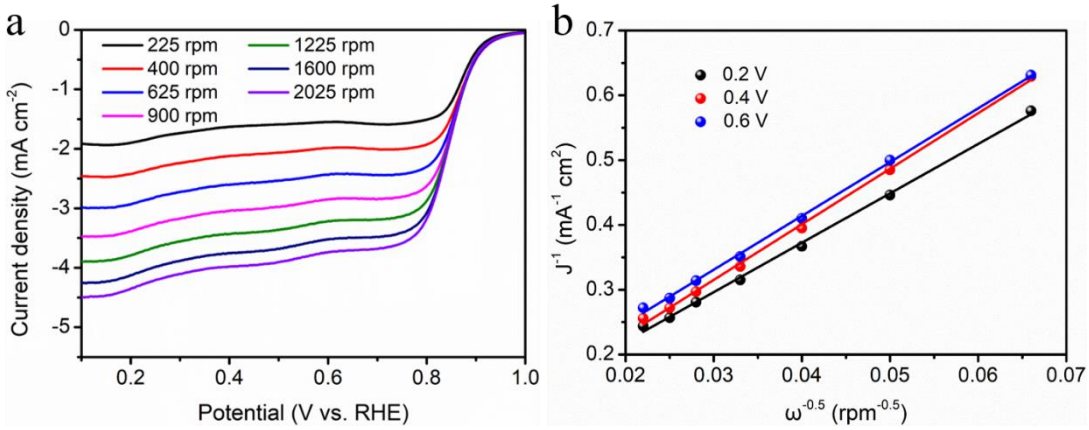

Figure S17. (a) LSV curves at different rotation speeds with a scanning rate of 10 mV s-1 and (b) the corresponding Koutecky-Levich plots at different electrode potential of commercial 40% Pt/C.

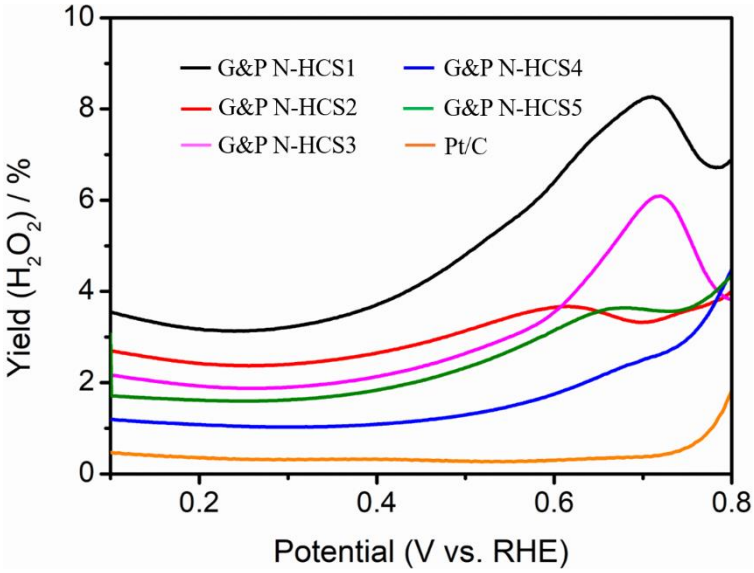

Figure S18. The H_2O_2 yield of G&P N-HCS1, G&P N-HCS2, G&P N-HCS3, G&P N-HCS4, G&P N-HCS5, and commercial JM 40% Pt/C calculated from RRDE plots at different electrode potential with a rotation speed of 1600 rpm.

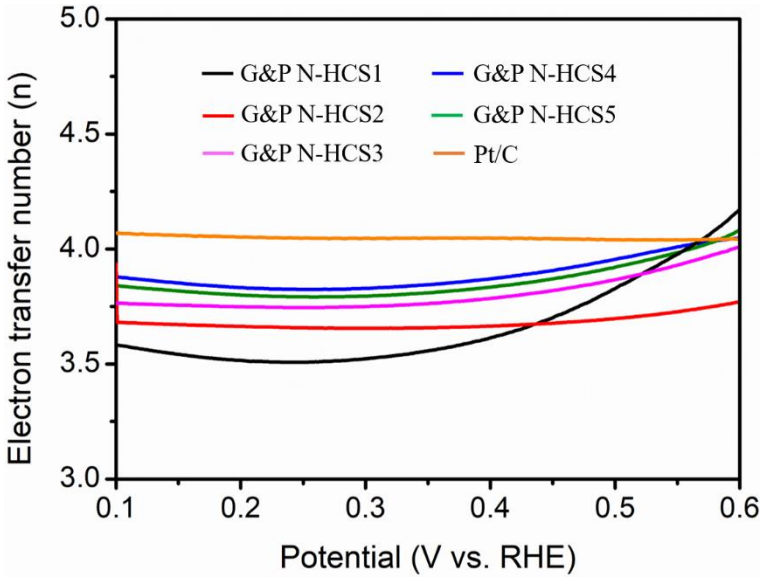

Figure S19. Electron transfer number (n) of G&P N-HCS1, G&P N-HCS2, G&P N-HCS3, G&P N-HCS4, G&P N-HCS5, and commercial JM 40% Pt/C calculated from H_2O_2 yield at different electrode potential.

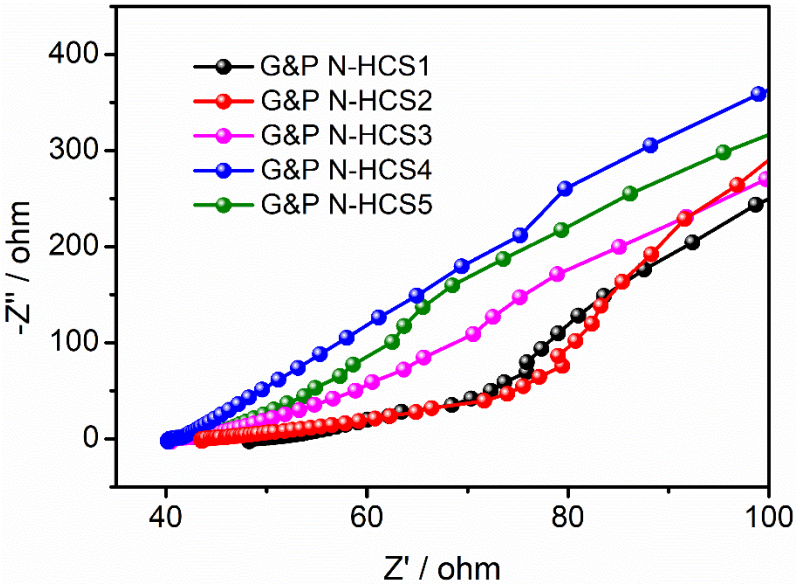

Figure S20. Electrochemical impedance spectroscopy (EIS) of G&P N-HCS1, G&P N-HCS2, G&P N-HCS3, G&P N-HCS4, and G&P N-HCS5.

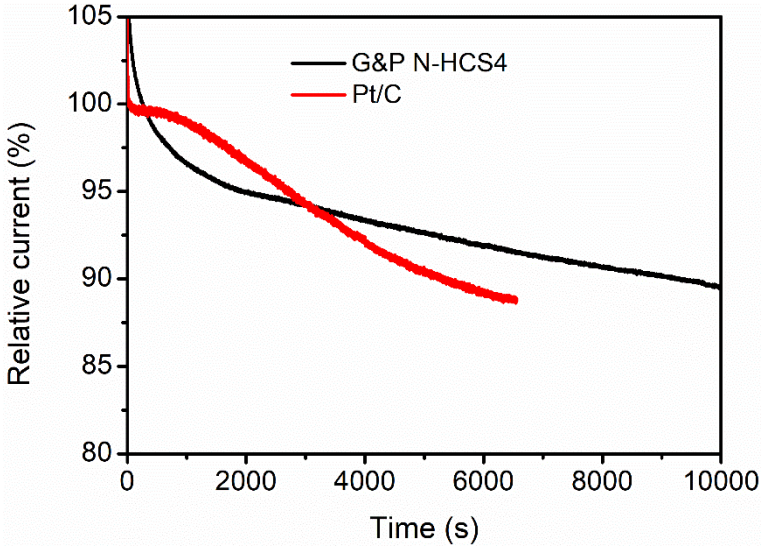

Figure S21. Relative i-t curves chronoamperometric response of G&P N-HCS4 and Pt/C at 0.7 V with a rotation speed of 1600 rpm.

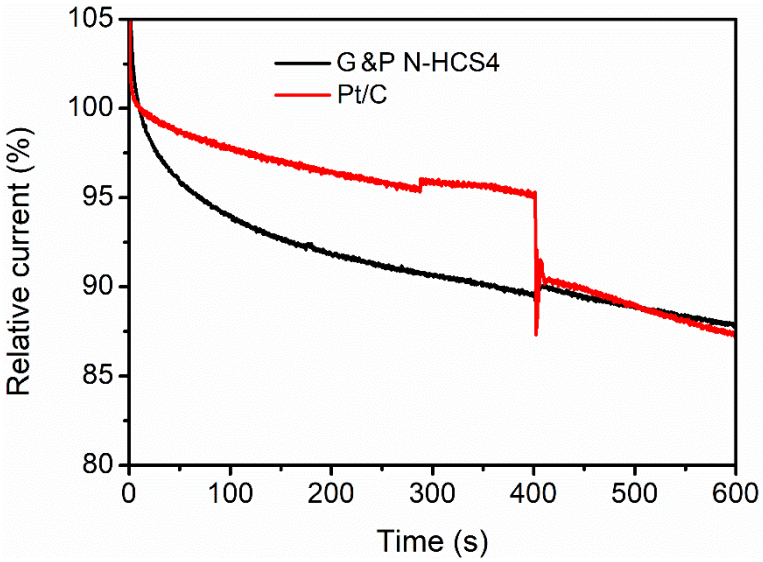

Figure S22. Current density-time (i-t) profiles of G&P N-HCS4 and Pt/C at 0.7 V in 0.1 M KOH (50 mL) with an addition of methanol (1 mL).

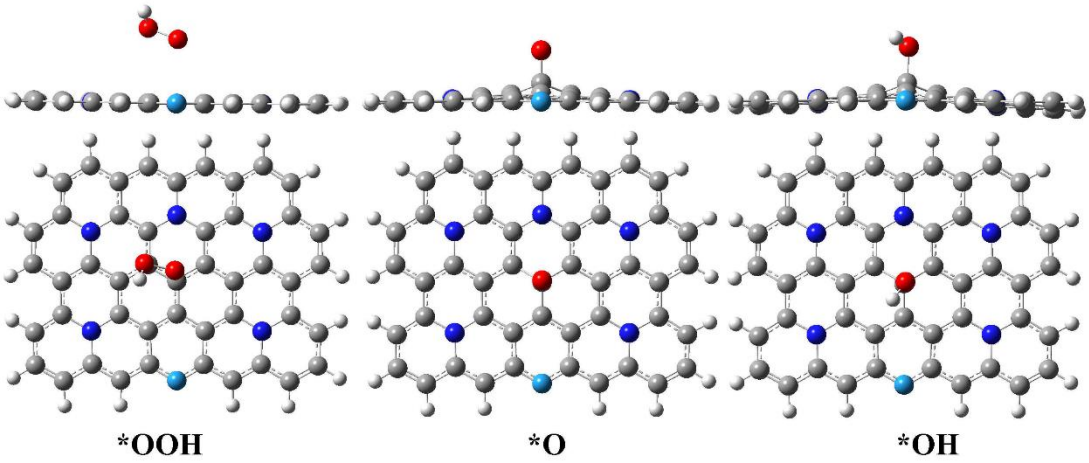

Figure S23. The optimized lowest atomic configurations of ORR intermediate states for 1PrN_5GrN in alkaline media.(O atom: red).

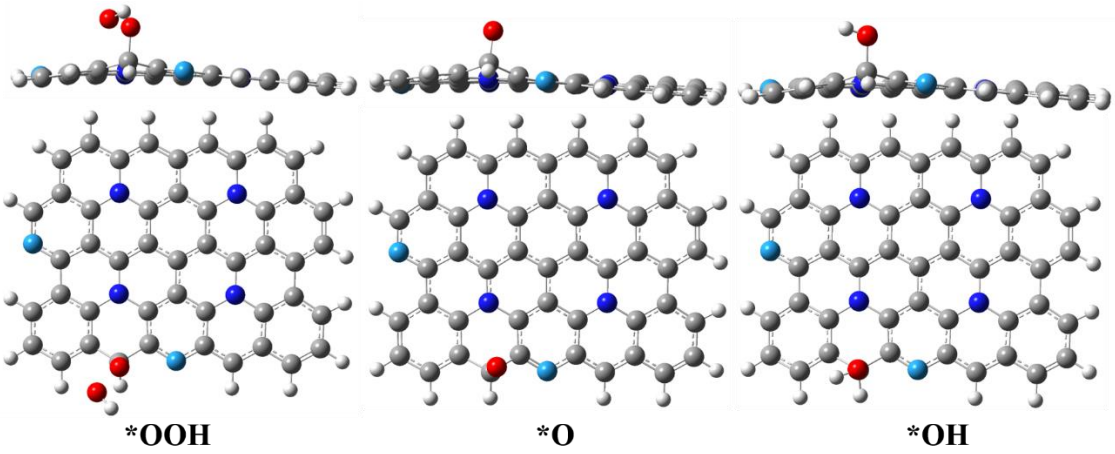

Figure S24. The optimized lowest atomic configurations of ORR intermediate states for 2PrN_4GrN in alkaline media.

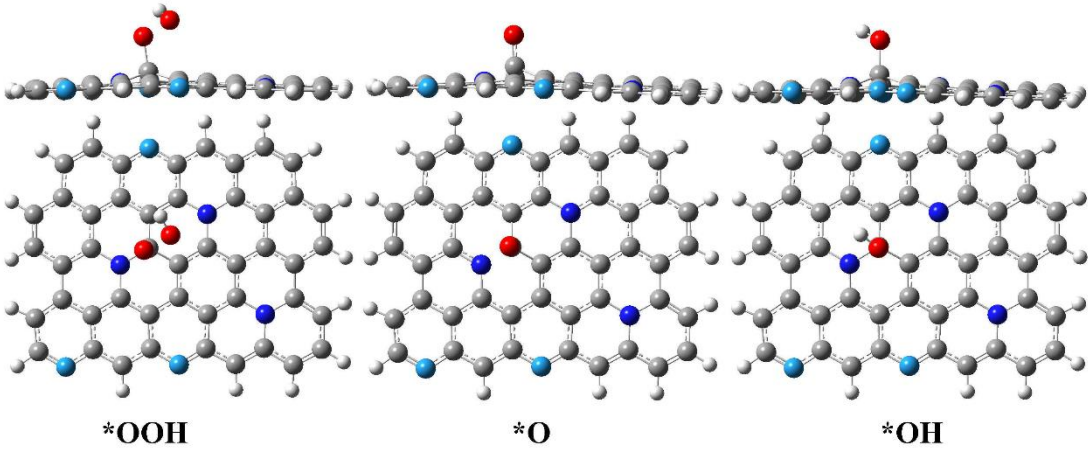

Figure S25. The optimized lowest atomic configurations of ORR intermediate states for 3PrN_3GrN in alkaline media.

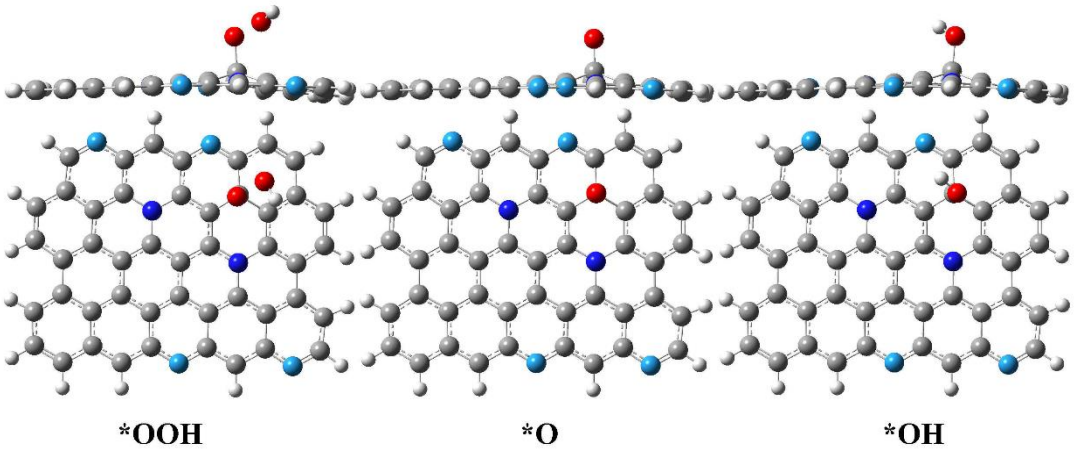

Figure S26. The optimized lowest atomic configurations of ORR intermediate states for 4PrN_2GrN in alkaline media.

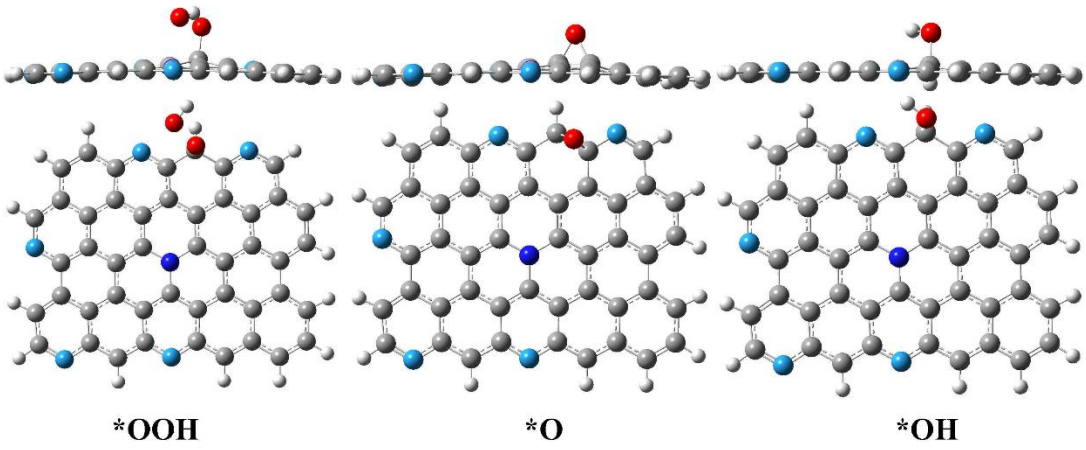

Figure S27. The optimized lowest atomic configurations of ORR intermediate states for 5PrN_1GrN in alkaline media.

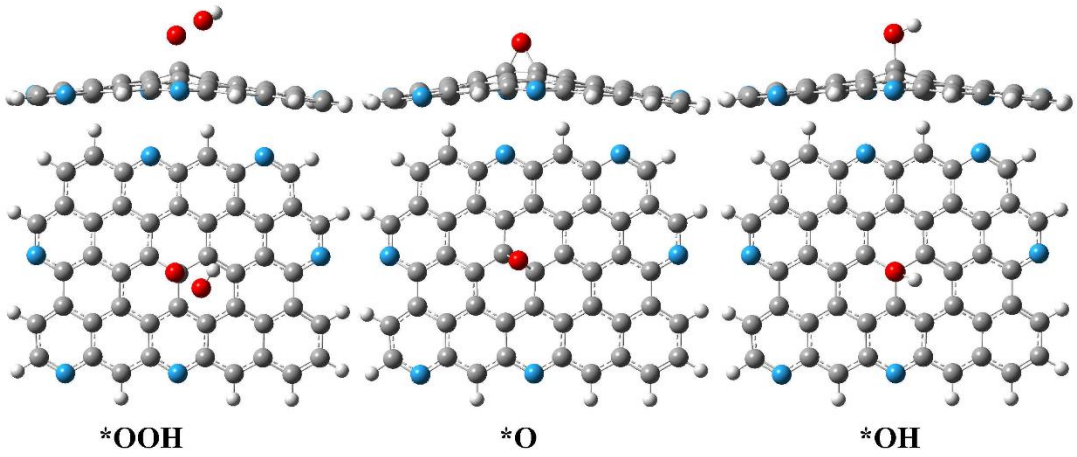

Figure S28. The optimized lowest atomic configurations of ORR intermediate states for 6PrN_0GrN in alkaline media.

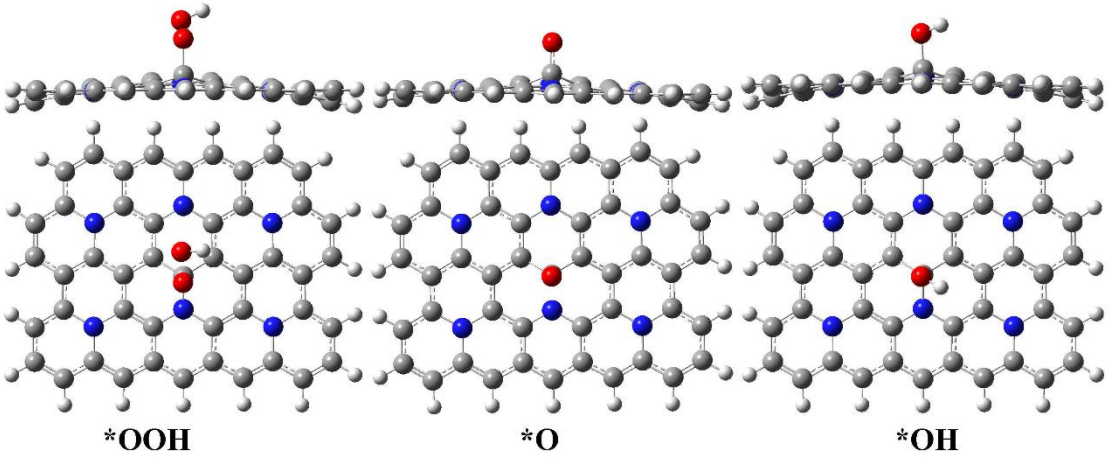

Figure S29. The optimized lowest atomic configurations of ORR intermediate states for 0PrN_6GrN in alkaline media.

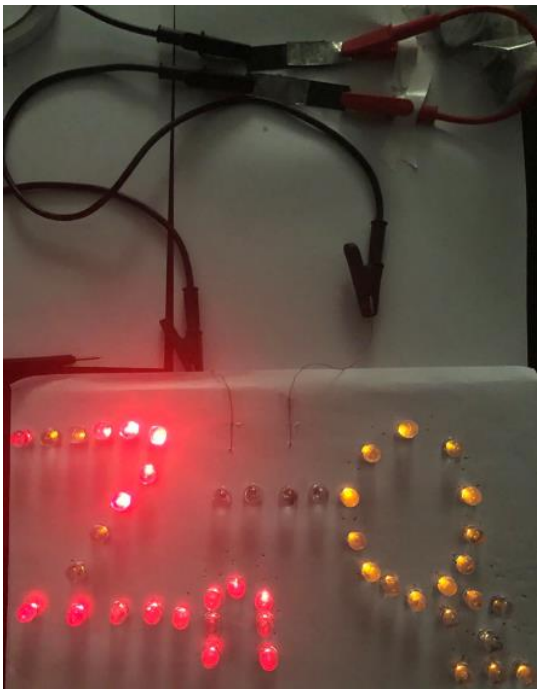

Figure S30. A paragraph of a pattern composed of LEDs being powered by two solid-state Zn-air batteries connected in series.

Table S1. N contents in our samples measured by energy dispersive spectroscopy (EDS) and element analysis (EA) technology.

Samples	N content (wt. %)measured by EDS	N content (wt. %) measured by EA
HCS	5.2	5.5
N-HCS	7.8	8.1
G&P N-HCS1	9.2	9.3
G&P N-HCS2	9.8	10.3
G&P N-HCS3	11.4	11.6
G&P N-HCS4	12.8	13.2
G&P N-HCS5	12.6	13.3

Table S2. Textural parameters of various samples.

Samples	S_{BET}	S_{micro}	V_{total}	V_{micro}	Pore size
	(m^2 g^{-1})	(m^2 g^{-1})	(m^3 g^{-1})	(m^3 g^{-1})	(nm)
HCS	85	40	0.28	0.15	0.64
N-HCS	154	81	0.66	0.51	0.66
G&P N-HCS1	221	103	0.71	0.62	0.68
G&P N-HCS2	235	132	0.75	0.63	0.68
G&P N-HCS3	242	150	0.77	0.65	0.71
G&P N-HCS4	258	208	0.81	0.73	0.72
G&P N-HCS5	256	191	0.80	0.72	0.72

Table S3. HOMO, LUMO, and HOMO_LUMO energy gap (Unit/eV) on graphene model (Gr) and seven nitrogen-doped catalysts.

Catalyst	HOMO	LUMO	HOMO-LUMO gap
1PrN_5GrN	-3.71	-2.55	1.16
2PrN_4GrN	-4.17	-2.79	1.38
3PrN_3GrN	-4.29	-2.78	1.51
4PrN_2GrN	-4.65	-2.99	1.66
5PrN_1GrN	-4.85	-3.59	1.26
6PrN_0GrN	-5.58	-3.64	1.93
0PrN_6GrN	-3.59	-2.47	1.12
Gr	-4.72	-2.82	1.90

Table S4. The free energy of *O, *OH and *OOH on various nitrogen-doped catalysts.

Catalyst	ΔG_{*OOH}	ΔG_{*O}	ΔG_{*OH}
1PrN_5GrN	2.23	0.86	0.87
2PrN_4GrN	1.97	0.49	0.41
3PrN_3GrN	1.63	0.45	0.22
4PrN_2GrN	2.52	1.42	0.97
5PrN_1GrN	1.92	0.91	0.42
6PrN_0GrN	3.28	1.91	1.73
0PrN_6GrN	1.88	-0.56	0.31

Table S5. The free energy variation for each step of the ORR elementary reaction on various nitrogen-doped catalysts with pH=13 and U^{NHE}=0.46 V.

Catalyst	$O_2+H_2O+e^-$ $\rightarrow$*OOH+OH^-	*OOH+e^- $\rightarrow$*O+OH^-	*O+H_2O+e^- $\rightarrow$*OH+OH^-	*OH+e^- $\rightarrow$* +OH^-
1PrN_5GrN	0.85	-0.91	0.47	-0.41
2PrN_4GrN	0.59	-1.02	0.38	0.05
3PrN_3GrN	0.25	-0.72	0.23	0.24
4PrN_2GrN	1.14	-0.64	0.01	-0.51
5PrN_1GrN	0.54	-0.55	-0.03	0.04
6PrN_0GrN	1.90	-0.91	0.28	-1.27
0PrN_6GrN	0.50	-1.91	1.33	0.15

References:

[S1] M. J. Frisch, G. W. Trucks, H. B. Schlegel, G. E. Scuseria, M. Robb, J. R. Chesseman and H. Nakatsuji, Gaussian 09, revision D.01; Gaussian, Inc.: Wallingford CT, 2009.

[S2] T. Qin, J. Zhao, R. W. Shi, C. W. Ge, Q. Li. Ionic liquid derived active atomic iron sites anchored on hollow carbon nanospheres for bifunctional oxygen electrocatalysis. Chem. Eng. J. 2020, 399, 125656.